

Molecular gas in the system of merging galaxies Arp 299*

F. Casoli¹, M.-C. Willaime¹, F. Viallefond¹, and M. Gerin^{2,1}

¹ DEMIRM, Observatoire de Paris, 61 Av. de l'Observatoire, F-75014 Paris, France and UMR 8540 du CNRS

² Radioastronomie millimétrique, ENS, 24 Rue Lhomond, F-75231 Paris Cedex 05, France and UMR 8540 du CNRS

Received 7 October 1998 / Accepted 8 March 1999

Abstract. We present new observations of the merging system Arp 299 obtained with the IRAM Plateau de Bure interferometer. We have observed the $^{12}\text{CO}(1-0)$, $^{12}\text{CO}(2-1)$, $^{13}\text{CO}(1-0)$ and HCN(1-0) lines. For the $^{12}\text{CO}(1-0)$ line, short spacings were recovered by using 30m data; about half of the total flux is found in weak and extended emission filtered out by the interferometer.

The $^{12}\text{CO}(1-0)$ map shows three bright regions associated with the nuclei of the galaxies (IC 694=A and NGC 3690=B) and to a star-forming region, C-C', which contains about one-third of the CO emission, but also extended emission and several "filaments" joining the bright regions. We find a south-east extension (A2) in IC 694 which corresponds to bright H_2 and $\text{Br}\gamma$ emission. The $^{12}\text{CO}(2-1)$ map which has $0.7'' \times 0.6''$ resolution but does not include short spacings shows the same gross features and is dominated by extremely bright emission in the nucleus of IC 694.

Strong HCN emission is also observed in the nucleus of IC 694 (A), indicating the presence of large amounts of dense gas; weaker emission is found in B, C and C': the $^{12}\text{CO}/\text{HCN}$ ratio varies between 20 and 40 in the body of Arp 299, while it is about 7 in nucleus A. B is weak in $^{13}\text{CO}(1-0)$ emission, with a $^{12}\text{CO}/^{13}\text{CO}$ ratio of about 30, while A and C-C' exhibit more "normal" ratios (11–16). Globally, C, C' and A2 exhibit line ratios that are typical of galactic disks, while A and B are clearly peculiar, with in particular HCN stronger than ^{13}CO .

We find in the CO(1-0) line a regular velocity gradient over the south-east part of IC 694, which apparently extends to the C-C' region. The other regions of Arp 299 have more complex dynamics; from the high-resolution $^{12}\text{CO}(2-1)$ maps, we are able to locate the dynamical center of NGC 3690 at the position of the radiocontinuum peak. We see clear indications that there is some gas flowing between IC 694 and NGC 3690. The three main regions are then dynamically and physically connected. In Arp 299, gas transfers have thus already occurred at an early stage of the merger.

Key words: ISM: molecules – galaxies: individual: Arp 299; NGC 3690; Mkn 171; IC 694 – galaxies: intergalactic medium – galaxies: interactions

1. Introduction

Mergers and interactions are an essential phenomenon for the evolution of galaxies. Mergers of disk galaxies may play a crucial role in the formation of elliptical galaxies; they can be accompanied by major starbursts that exhaust most of the original gas content of the progenitors. Indeed, all ultraluminous infrared galaxies are now recognized to be strongly interacting or merging objects (e.g. Clements & Baker 1996, Clements et al. 1996).

The gas dynamics and the associated star formation clearly play a key role during these transformations of galaxies. For example, a large fraction of these ultraluminous galaxies seem to harbor an active nucleus (Goldader et al. 1997), although the fraction of the infrared luminosity which is powered by the AGN is a matter of some debate, see e.g. Smith et al. (1998); this frequent association is probably due to gas accumulation in the central region. Numerical simulations begin to be able to study these phenomenon and to include a crude description of star formation (e.g. Mihos & Hernquist 1996, Barnes & Hernquist 1996). However, much has still to be learned from the observations: what are the processes which transfer the gas in the inner regions of the galaxies? Is the starburst confined to the nuclei? What is the importance of extranuclear star forming regions?

Arp 299 (Mkn 171) appears to be a good target to understand how star formation and gas transfer proceed during the late stages of the interaction, before the final merging. This is one of the nearest mergers, at a distance of 42 Mpc (for $H_0 = 75 \text{ km s}^{-1} \text{ Mpc}^{-1}$; at this distance, $1'' = 204 \text{ pc}$). It is composed of two main bodies, IC 694 (=A) to the east and NGC 3690 (=B) to the west (see Fig. 1; other images in Casoli et al. 1989 and Hibbard & Yun 1996; 1.5 GHz maps in Condon et al. 1990 and 8 GHz maps in Zhao et al. 1997). Arp 299 is not a genuine "ultraluminous" galaxy but still, it has a far-infrared luminosity of $3.7 \cdot 10^{11} L_{\odot}$ (Casoli et al. 1992). In the optical images there are no obvious tidal tails but Hibbard & Yun (1996, 1999) have found two huge HI tails (180 kpc in length) as well as a faint

Send offprint requests to: F. Casoli (Fabienne.Casoli@obspm.fr)

* Based on observations carried out with the IRAM Plateau de Bure Interferometer. IRAM is supported by INSU/CNRS (France), MPG (Germany) and IGN (Spain).

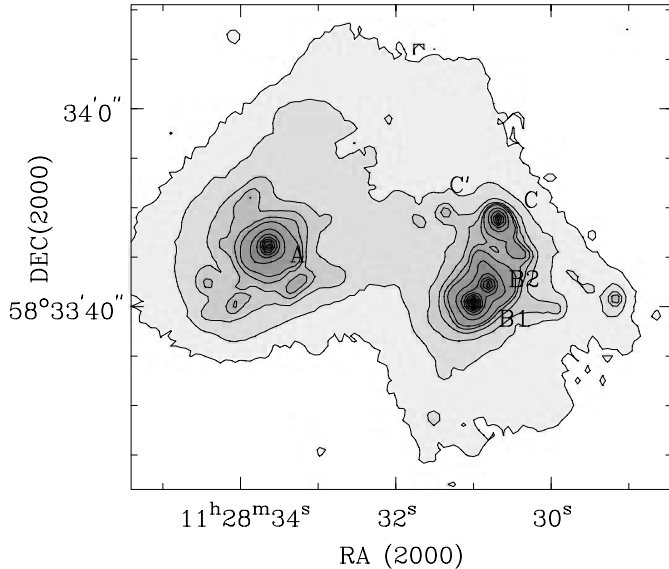


Fig. 1. Map of the Arp 299 system at $2.1 \mu\text{m}$, obtained with the CFHT telescope. Seeing $\simeq 1''$. See Willaime et al., in preparation, for details. The region A is the nucleus of IC 694, B1 and B2 are associated with NGC 3690 (the nucleus of which is probably B1), C could be a huge extra-nuclear star-forming region or a third galaxy nucleus, while C' is a star-forming region. A, B1, C and C' are clearly seen in radio and CO maps while B2 is not. This figure and the following ones, except Fig. 9, Fig. 10, Fig. 11, Fig. 13 and Fig. 14 are drawn to the same scale.

optical one curiously displaced from each other. They suggest that the encounter is rather old ($\simeq 750$ Myr).

Because of dust extinction, it is difficult to locate the nuclei from optical images. Radio and infrared observations by Gehrz et al. (1983) have uncovered four main regions of activity, labelled A, B (B1/B2 in Fig. 1, see below), C and C'. These regions can be recognized in Fig. 1 which is a narrow-band continuum $2.1 \mu\text{m}$ picture taken with the CFHT (see Willaime et al., in preparation, for details). A is associated with the nucleus of IC 694 and may harbor an active nucleus since it is a flat-spectrum radio-source (Gehrz et al. 1983). C could either be an extranuclear star forming region, although of an extraordinary strength (Dudley & Wynn-Williams 1993, Keto et al. 1997), or the nucleus of a third galaxy (Casoli et al. 1989). C' is clearly a star-forming region. Region B likely contains the nucleus of NGC 3690; the separation between the nuclei of the two main galaxies is then $22'' = 4.5$ kpc.

However, in the NIR images (e.g. Fig. 1), B is split in 2 sources, B1 and B2, and it is not clear which one is the dynamical center of the galaxy (Smith et al. 1996, Wynn-Williams et al. 1991). Shier et al. (1996) find that the $2 \mu\text{m}$ spectrum of B1 could be fitted by an active nucleus, while that of B2 could be that of a 60 Myr old starburst. B2 is marginally detected at mid-IR wavelengths (Keto et al. 1997) but not at all in radio maps, and thus could correspond to a population of post-AGB stars; the true nucleus of NGC 3690 would then be B1.

As for its gaseous content, Arp 299 contains $9.6 \cdot 10^9 M_{\odot}$ of atomic gas, of which $6.3 \cdot 10^9 M_{\odot}$ is in the main body and the rest in the tidal tails (Hibbard & Yun 1996, 1999). There have been

Table 1. Observational parameters. In column 2, (u) is for uniform weighting, (n) is for natural.

Line	beam	PA	dV km s^{-1}	rms noise mJy/beam
$^{12}\text{CO}(1-0)$	$3.7'' \times 2.5''$ (u)	71°	6.58	10
$^{13}\text{CO}(1-0)$	$3.2'' \times 2.5''$ (u)	23°	15.0	1.8
HCN(1-0)	$2.95'' \times 2.85''$ (n)	239°	20.0	0.6
$^{12}\text{CO}(2-1)$	$0.73'' \times 0.62''$ (u)	72°	9.86	8

numerous studies of the molecular gas distribution in this object, either with single-dish telescopes or interferometers (Solomon & Sage 1988, Casoli et al. 1989, Sargent et al. 1987, Sargent & Scoville 1991). The $^{13}\text{CO}(1-0)$ emission is found to be weak in Arp 299 with respect to $^{12}\text{CO}(1-0)$, as it has been found in other mergers, with an average emissivity ratio in the (1-0) line of about 20 (Aalto et al. 1991, Casoli et al. 1992). Aalto et al. (1997) have recently mapped $^{12}\text{CO}(1-0)$, $^{13}\text{CO}(1-0)$ and HCN(1-0) emissions of Arp 299 using the Owens Valley Radio Interferometer. The $^{12}\text{CO}(1-0)$ emission is found to peak on the main regions, A, B, C and C', with low-surface brightness extended emission south of A, east of C', and possibly a disk around B. $^{13}\text{CO}(1-0)$ emission is found to peak outside the nuclei, while the HCN emission is bright on the nuclei.

Here we present new observations of these lines using the IRAM instruments: the Plateau de Bure interferometer and the 30m telescope. These observations are described in Sect. 2; Sect. 3 describes the observed morphology in the $^{12}\text{CO}(1-0)$ and $^{12}\text{CO}(2-1)$ lines, Sect. 4 presents the observations of the other molecules and Sect. 5 deals with the gas dynamics. Sect. 6 presents a discussion of the results and our conclusions.

2. Observations and data reduction

2.1. Plateau de Bure observations

The $^{12}\text{CO}(1-0)$ observations have been carried out during the winter 1994-1995. The Plateau de Bure interferometer was at that time composed of 4 antennas (see Guilloteau et al 1992) and we used the CD configuration (actually, a set of 3 configurations: D, C2, C1) with baselines from 24 to 161 m. This led to a resolution of $3.7'' \times 2.5''$ for uniform weighting (beam PA = 71°). The galaxy was observed with a mosaic of two overlapping fields, the first one centered on the position $\alpha(2000) = 11\text{h } 28\text{min } 34.8\text{ s}$, $\delta(2000) = 58^{\circ} 33' 50''$, and the second one at $(-1'', 0'')$ offsets. The correlator setup yielded a frequency resolution of 2.5 MHz (6.57 km s^{-1}) and a 423 MHz bandwidth (2780 km s^{-1}) centered on the frequency $\nu = 114.076 \text{ GHz}$ (which corresponds to $v_{\text{hel}} = 3140 \text{ km s}^{-1}$). The main characteristics of these observations are given in Table 1.

The $^{13}\text{CO}(1-0)$ observations have been carried out during the winter 1995-1996, with 4 antennas in the CD configuration. This led to a resolution of $3.2'' \times 2.5''$ for uniform weighting (beam PA = 23°). The galaxy was observed with a mosaic of four fields, the first one centered on the position $\alpha(2000) = 11\text{h } 28\text{min } 32.5\text{ s}$, $\delta(2000) = 58^{\circ} 33' 46''$, and the others at $(9'',$

0''), (-12'', 4'') and (-12'', -6'') offsets. The correlator setup yielded a frequency resolution of 2.5 MHz (6.87 km s⁻¹) and a 380 MHz bandwidth (2610 km s⁻¹) centered on the frequency $\nu = 109.021$ GHz (which corresponds to $v_{\text{hel}} = 3245$ km s⁻¹).

The HCN(1–0) observations have been carried out during the winter 1996–1997, with 5 antennas, using the B1, B2, C2 and D1 configurations for a maximum baseline of 273 m. This led to a resolution of 2.95''x2.85'' for natural weighting (beam PA = 239°). The galaxy was observed with a mosaic of five fields at offsets (-4'', 0''), (6'', 0''), (-12'', 4''), (-12'', -6'') and (14'', -6'') with respect to $\alpha(2000) = 11\text{h } 28\text{min } 32.5\text{ s}$, $\delta(2000) = 58^\circ 33' 46''$. The correlator setup yielded a frequency resolution of 2.5 MHz (8.54 km s⁻¹) and a 270 MHz bandwidth (2306 km s⁻¹) centered on the frequency $\nu = 87.713$ GHz (which corresponds to $v_{\text{hel}} = 3138$ km s⁻¹).

The ¹²CO(2–1) observations were carried out during the winters 1996–1997 and 1997–1998, using the A, B1, B2, C2 and D1 configurations for a maximum baseline of 408m. This led to a resolution of 0.73''x0.62'' for natural weighting (beam PA = 72°). The five-field mosaic was the same as for the HCN observations. The correlator setup yielded a frequency resolution of 2.5 MHz and a bandwidth of 500 MHz centered on the frequency $\nu = 228.148$ GHz (which corresponds to $v_{\text{hel}} = 3140$ km s⁻¹).

For the four data sets, phase and amplitude calibration were achieved using several continuum sources: 0923+392, 0954+556, 1044+719, 1150+497. Bandpass and flux calibration were done on 3C273, of which the flux density is monitored regularly against planets.

The data were calibrated using the CLIC and GILDAS softwares developed at IRAM and Observatoire de Grenoble. Images were produced using uniform weighting (for ¹²CO, ¹²CO(2–1) and ¹³CO) or natural weighting (for HCN). Cleaned mosaics were produced by performing a joint deconvolution of the different fields. The datacubes were further processed using the GIPSY package.

2.2. Single-dish ¹²CO(1–0) observations

Additional ¹²CO(1–0) observations were obtained at the IRAM 30m telescope in June 1996, in order to recover the short spacings. The line was observed simultaneously with two SIS receivers with single-sideband system temperatures of about 350 K (T_A^{*} scale). We used two backends of 512 contiguous 1 MHz filters (2.6 km s⁻¹).

The observing mode was the following: we have observed 130 positions with a 4'' sampling in a region chosen to cover the two-fields mosaic of the Plateau de Bure observations. On each position, we have taken between two and six scans, each of one minute duration; since the observing mode was wobbler switching (with a 100'' throw), this means that the integration time on each position varied between 60 and 180 s. The integration time on each position varied between 1 and 3 min; it was chosen to mimic the noise in the interferometer map so that the central positions were observed with an on-source integration time of 3 min and the outer ones, 1 min.

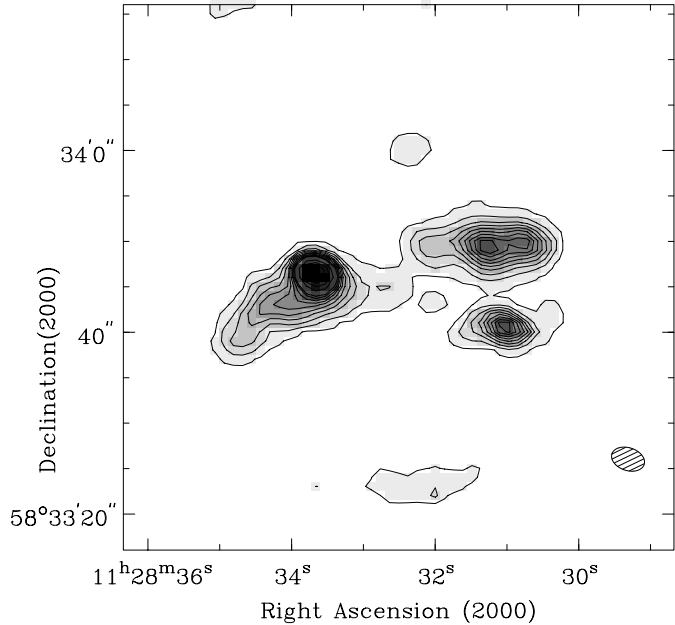


Fig. 2. Map of the ¹²CO(1–0) line area (zeroth-order moment computed from 2890 to 3330 km s⁻¹) from the interferometer observations alone. Beam size is indicated in the lower right corner. Levels: 0.5 to 30 Jy km s⁻¹/beam by steps of 3, then 40, 50, 60 Jy km s⁻¹/beam.

The spectra were transformed into a single-dish data base that can be handled by GIPSY, then reduced using tasks developed by one of us (FV) in the GIPSY package. Linear baselines were removed and the spectra were edited for bad channels. We then built a datacube at 1'' resolution; blank pixel values were replaced by interpolated values derived from the nearest observed points. The last step was to filter out the high-frequency noise due to the oversampling of the observations.

2.3. Combining PdB and 30m data

The combination of the interferometer and single-dish data was done using the task RELCAL in the GIPSY environment. From the single dish image, this task synthesizes visibilities at the resolution of the array. It checks for the relative calibration between the single dish and array visibilities, and then puts these synthesised visibilities together with those from the array using the appropriate weights.

The interferometer map of the first moment of the ¹²CO(1–0) line is shown in Fig. 2, and the combined map in Fig. 3. It is clear from the comparison of Fig. 2 and Fig. 3 that Arp 299 contains widespread low-brightness ¹²CO(1–0) emission which was not detected by the interferometer. The total flux in the PdB map is about 296 Jy km s⁻¹ while that in the 30m map is 630 Jy km s⁻¹; this means more than half of the total emission originates from a weak extended component which was filtered out by the array.

This result can be compared to that of Aalto et al. (1997). The total ¹²CO(1–0) flux in the OVRO map is 354 Jy km s⁻¹. As expected, this is slightly more than what we see at PdB but

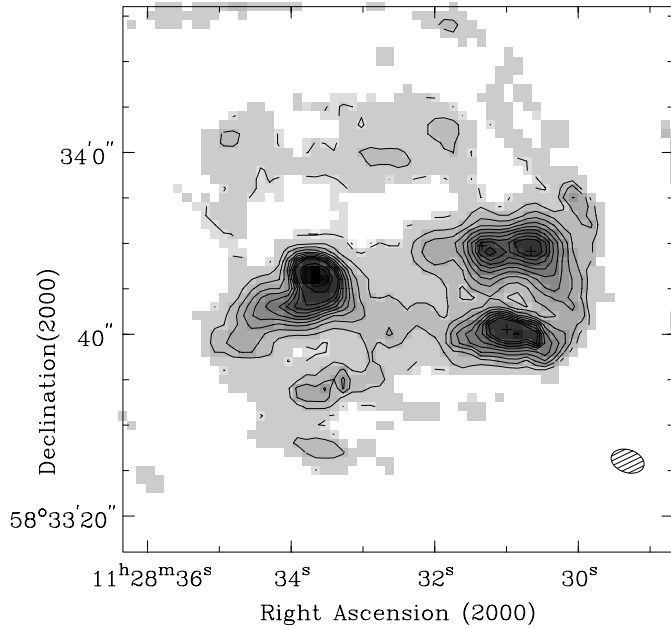


Fig. 3. Map of the velocity integrated $^{12}\text{CO}(1-0)$ profiles (zeroth order moment, computed from 2890 to 3330 km s^{-1} ; the integration range is the same for the other lines) from the 30m observations combined with the interferometer data. Beam size ($3.7'' \times 2.5''$) is indicated in the lower right corner of the map. Levels: 0.1, 0.2, 0.5 to 30 $\text{Jy km s}^{-1}/\text{beam}$ by steps of 3, then 40, 50, 60 $\text{Jy km s}^{-1}/\text{beam}$. Crosses mark the positions of A, B1, C and C' (see Fig. 1)

less than the total 30m flux. The total H_2 mass in Arp 299 from our data is then $M_{\text{H}_2} = 1.0 \cdot 10^{10} M_{\odot}$ for a conversion factor $X = N(\text{H}_2)/I(\text{CO}) = 2.3 \cdot 10^{20} \text{ mol cm}^{-2}/\text{K km s}^{-1}$ and a distance of 42 Mpc. Out of these $10^{10} M_{\odot}$, about 30 percent are associated with IC 694 (A), 30 percent with the C-C' region, 20 percent with B and the remaining 20 percent are widespread molecular gas (these are rough numbers since given the object morphology, it is not easy to draw frontiers between the galaxies). The interesting point here is that about one third of the emission is found in the C-C' region which is not clearly associated with any of the nuclei.

2.4. Continuum emission

The continuum map at 87.7 GHz (which does not include short spacings) is shown in Fig. 4. The four main regions, A, B, C and C' are clearly detected but also extended emission around them. We had to take care of this strong continuum when producing the $^{13}\text{CO}(1-0)$ and HCN maps, since in both cases the continuum is not negligible compared to the line emission. Continuum subtraction was achieved by using the task CONREM in GIPSY: a constant value for the continuum was fit using channels free of line emission, then a continuum-free line datacube and a continuum map were produced.

Table 2 gives the continuum flux densities at 87.7 and 109.02 GHz, from the HCN and $^{13}\text{CO}(1-0)$ data respectively. The first and last column give for comparison the values at 8.3 GHz determined by Zhao et al. (1997) and those at 110 GHz

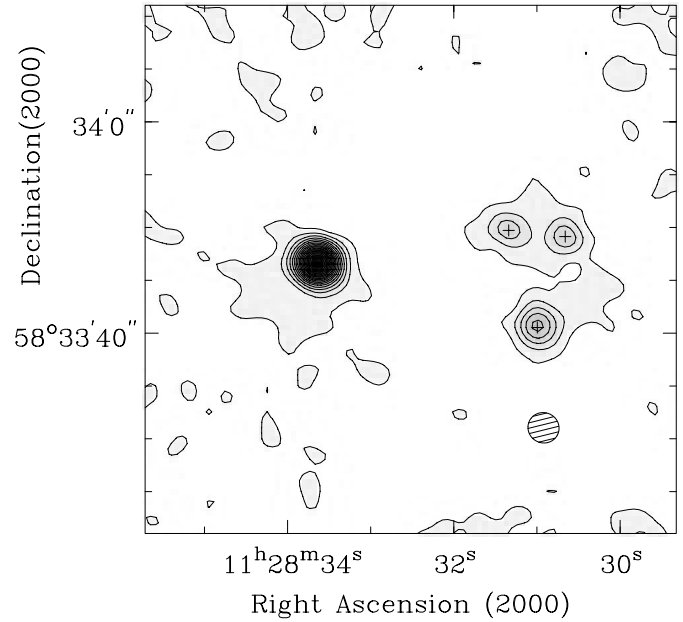


Fig. 4. Map of the continuum emission detected at 87.7 GHz. Beam size ($2.95'' \times 2.85''$) is indicated in the lower right corner of the map. Levels: 0.5 mJy/beam to 20 mJy/beam by steps of 1 mJy/beam. Crosses mark the positions of A, B1, C and C' (see Fig. 1)

Table 2. Continuum sources in the Arp 299 system

Source	S(8.3) (mJy)	S(87.7)	S(109.2)	S(110)
A	77.6 ± 1	23.5 ± 1	21 ± 1	17 ± 2
B	13 ± 0.5	6 ± 1	5 ± 1	5 ± 2
C	–	3 ± 1	1.5 ± 1	9 for C – C'
C'	–	4 ± 1	3 ± 1	

found by Aalto et al. (1997). From the flux densities observed at 8.3 and 87.7 GHz, we derive a spectral index of -0.51 ± 0.02 for A and -0.41 ± 0.10 for B.

3. Morphology of the CO emission

Fig. 3 exhibits two kinds of structure: bright, concentrated emission in the main regions, A, B1, C and C', but also weak and extended emission spread over the whole Arp 299 body. A is the brightest region, with an extension to the SE (A2 in the notation by Aalto et al. 1997) which is, to the resolution of these observations, associated with a bright filament seen in H_2 and $\text{Br}\gamma$ emission (Willaime et al., in preparation), but also to a ridge of radio continuum emission in the 8.3 GHz maps of Zhao et al. (1997). In general, the overall agreement with the IR emission lines maps is rather good. Not totally surprisingly, at the $2''$ scale (400 pc), molecular clouds and regions of massive star formation are closely related. This bright filament is also seen in H–K and J–H extinction maps by Shier et al. (1996); these maps show good agreement with our interferometer ^{12}CO map except maybe for B, where the extinction has a rather round shape

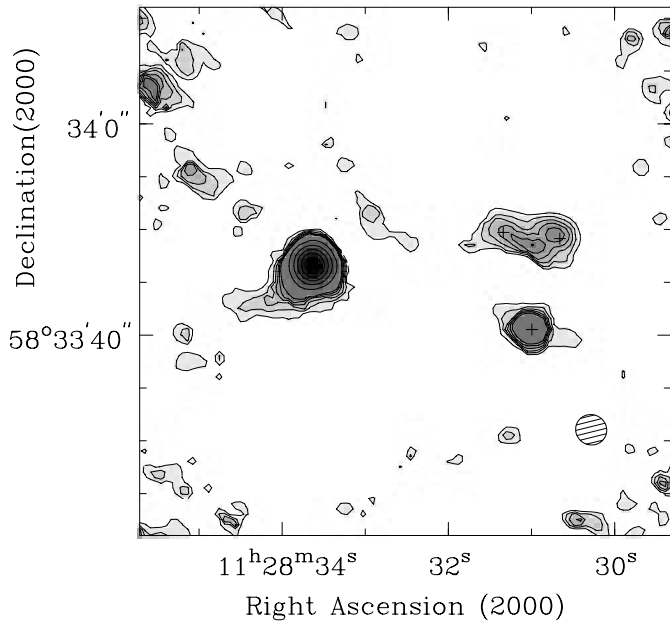


Fig. 5. Map of the zeroth-order moment of the HCN(1–0) line profile. Beam size ($2.95'' \times 2.85''$) is indicated in the lower right corner of the map. Levels and grayscale: 0.07, 0.15, 0.25, 0.4, 0.6 to 6 $\text{Jy km s}^{-1}/\text{beam}$ by steps of 0.6. Crosses mark the positions of A, B1, C and C' (see Fig. 1)

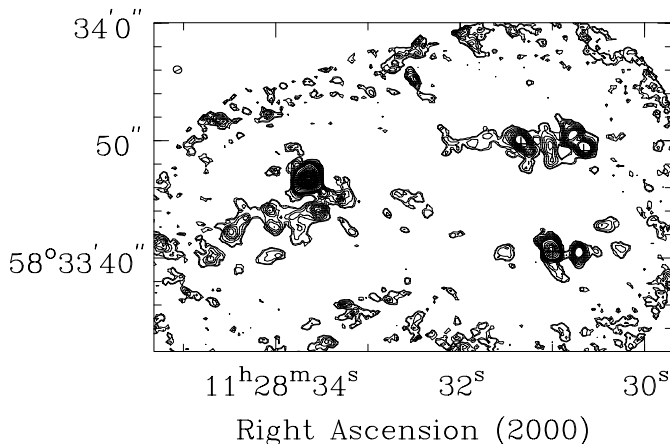


Fig. 6. Map of the zeroth-order moment of the CO(2–1) line profile. Beam size ($0.73'' \times 0.62''$) is indicated in the upper left corner of the map. Contour levels: 0.7, 1 to 10 $\text{Jy km s}^{-1}/\text{beam}$ by steps of 1, 15 to 50 $\text{Jy km s}^{-1}/\text{beam}$ by steps of 5, then 60 to 150 $\text{Jy km s}^{-1}/\text{beam}$ by steps of 10.

compared to the disk-like structure seen in the $^{12}\text{CO}(1-0)$ map.

C and C' are clearly seen, as well as a weaker concentration East of C'. We confirm two weak structures seen in the OVRO map by Aalto et al. (1997): the filament F joining A and B, and their region D to the North, at velocities between 3150 and 3300 km s^{-1} . However, with the combined 30m-PdB map we can see now that D and F are actually bright spots inside the diffuse envelope of molecular emission in which Arp 299 is embedded.

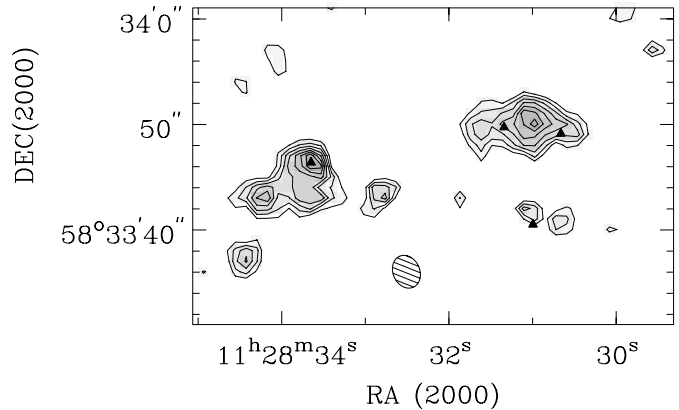


Fig. 7. Map of the zeroth-order moment of the $^{13}\text{CO}(1-0)$ line profile. Beam size ($3.2'' \times 2.5''$) is indicated by the hatched ellipse in the lower part of the map. Levels: 0.7 to 5 $\text{Jy km s}^{-1}/\text{beam}$ by steps of 0.3. Triangles mark the positions of A, B1, C and C' (see Fig. 1)

Fig. 6 shows the distribution of the $^{12}\text{CO}(2-1)$ line (integrated intensity). These high-resolution observations do not include short spacings and are only sensitive to small-scale emission. The most prominent feature is the very strong emission in A (IC 694); B1 (NGC 3690) is also a peak of emission but to a lesser degree. The C–C' regions are much weaker. The $^{12}\text{CO}(2-1)$ map thus bears a strong resemblance to that of HCN. There is also weak and knotty emission associated with region A2 and closely associated to the “filaments” of emission seen in H_2 and $\text{Br}\gamma$. The disk-like structure seen in NGC 3690 in the $^{12}\text{CO}(1-0)$ map is now resolved and appears to be composed of a concentration around the radiocontinuum peak (B1) and of two knots of emission east and west of B1. Because of their much higher resolution and the fact that they do not include short spacings, these observations cannot easily be compared with those of other lines. In a forthcoming paper, we will present a quantitative comparison with the NIR CFHT observations and HST archival data.

4. $^{13}\text{CO}(1-0)$ and HCN(1-0)

4.1. Distributions

The map of the integrated intensity of the $^{13}\text{CO}(1-0)$ line is shown in Fig. 7, while that of HCN(1–0) is given in Fig. 5. The overall distributions are rather similar to that of $^{12}\text{CO}(1-0)$. However, there are some important differences between the 3 lines: the HCN(1–0) line, for which we have the best angular resolution, peaks very clearly on A, B, C and C'. It is extremely strong in A. On the other hand, $^{13}\text{CO}(1-0)$ emission peaks in between C and C', has a strong maximum on A, and is just detectable on B.

4.2. Short spacings

In the following, we will discuss only the small-scale emission, in the absence of single-dish images for these two lines. The

question however arises if we could miss a large fraction of the flux by not including short spacings.

The HCN(1–0) line has been observed with the 30m telescope by Solomon et al. (1992). They have used two pointings, one close to A and the second one close to C; the beamsize of the 30m telescope being $27''$ at the HCN(1–0) frequency, there is some overlap between the two positions that are distant by $21''$. On A they found a flux of $13.8 \text{ Jy km s}^{-1}$ (we use a value of 6 for the Jy/K conversion factor at this frequency) and $16.8 \text{ Jy km s}^{-1}$ on the second position; if we integrate our map in $27''$ diameter regions centered on the same positions, we find respectively 15 and 8 Jy km s^{-1} . The total flux in the map is 17 Jy km s^{-1} . Given the uncertainties (their spectrum on A is rather noisy and the one on C is not shown), there is no strong evidence that there is missing flux in our HCN map.

As for ^{13}CO , we have used 30m $^{13}\text{CO}(1-0)$ data taken in the same way as for the ^{12}CO short spacings to compute the $^{13}\text{CO}(1-0)$ flux around A. Because of small pointing uncertainties due to poor weather, these maps are not of sufficient quality to be used as short spacings but they should give a good indication of total fluxes. We find 19 Jy km s^{-1} , to be compared to the PdB value, 18 Jy km s^{-1} . Here again, there is no significant missing flux.

Note that the fact that with the 30m telescope, the flux found on A are about equal for HCN and ^{13}CO is not in contradiction with the line ratios given in Table 3. These values are given for a $3''$ region around the nucleus, while those for the 30m refer to the whole single-dish beam, which encompasses regions like the A2 extension, where ^{13}CO is stronger than HCN.

4.3. Comparison with previous observations

The IRAM $^{13}\text{CO}(1-0)$ map of Arp 299 disagrees with the OVRO map (Aalto et al. 1997) especially for A. As for C and C', our results are in better agreement. Line ratios are difficult to compare quantitatively, since our ^{12}CO map includes short-spacings. We believe that the differences can be attributed to different ways of subtracting the continuum emission. Indeed this subtraction is a delicate operation since the continuum is several times stronger than the line. Depending on the correlator configuration there may not be many channels to estimate the continuum level. The differences with Aalto et al. (1997) could be understood if we have subtracted too little continuum emission for A, but a look at Table 2 shows that it is probably not the case: the 109 GHz flux density that we compute for A is higher than that quoted by Aalto et al.

To explore further this discrepancy, we have made several checks of our ^{13}CO map. This line was observed again during the winter 1997–1998 in AB configuration; the beamsize is $1.34'' \times 1.26''$. This map has a lower signal to noise ratio than the previous one but the main features remain: emission at the position of the IC 694 nucleus (A), two blobs of emission associated with C and C', very weak emission on B. There are small displacements of the emission peaks from the continuum sources for C' in particular that seem real and correspond to structures seen in the higher resolution CO(2–1) map.

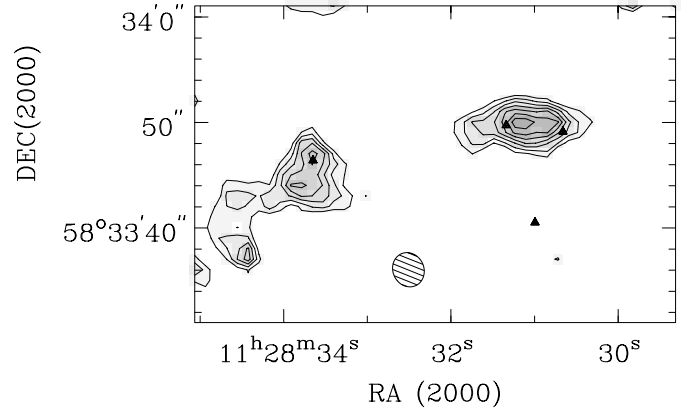


Fig. 8. ^{13}CO map produced by subtracting the 87.7 GHz continuum, extrapolated to 109.02 GHz using a spectral index of -0.5 , to the ^{13}CO datacube. Levels are as in Fig. 7. Note the good overall correspondance between this map and Fig. 7, despite a small difference in beamsizes, and the fact that the spectral index could vary over the map.

Table 3. Integrated brightness temperature ratios in the Arp 299 system, at a resolution of $3.8''$

Lines	A	B	C	C'	A2
CO/ ^{13}CO	24 ± 2	29 ± 3	16 ± 1	11 ± 2	10 ± 1.5
CO/HCN	7 ± 1	20 ± 1	45 ± 8	29 ± 2	20 ± 2
$^{13}\text{CO}/\text{HCN}$	0.3 ± 0.05	0.6 ± 0.1	2.5 ± 0.4	2.5 ± 0.2	1.8 ± 0.1

We made a second check by using the continuum map at 87.7 GHz derived from the HCN observations to subtract the continuum emission from the ^{13}CO data cube. To do this we extrapolated the map shown in Fig. 4 using a spectral index of -0.5 , which is well suited to nucleus A. This should give reasonable results, first because this represents only a small frequency extrapolation; second, because the 87.7 GHz continuum is well defined, owing to the larger number of line-free channels and the good signal-to-noise ratio (see Fig. 4). The resulting continuum-free ^{13}CO map is shown in Fig. 8; its spatial resolution is $3.3'' \times 2.9''$, thus slightly worse than that of Fig. 7. The two maps show essentially the same structures; both exhibit a maximum of emission on A. The differences, in particular around B, can be attributed to the spatial variations of the spectral index of the continuum emission.

Braine & Dumke (1998) have mapped the 1.3mm dust continuum emission using the IRAM 30m telescope. They find that the emission is strongly peaked on A and that there is twice as much emission in this region as in the (B+C+C') region (their beamsize is $11''$). Since the dust continuum emission traces the bulk of the gaseous mass, these data support the presence of a large mass of molecular gas in A.

4.4. Line ratios

To compute line ratios, we have smoothed all three maps to a common resolution of $3.8'' \times 3.8''$ (770 pc). The values of ratios of the integrated brightness temperature at the positions of A,

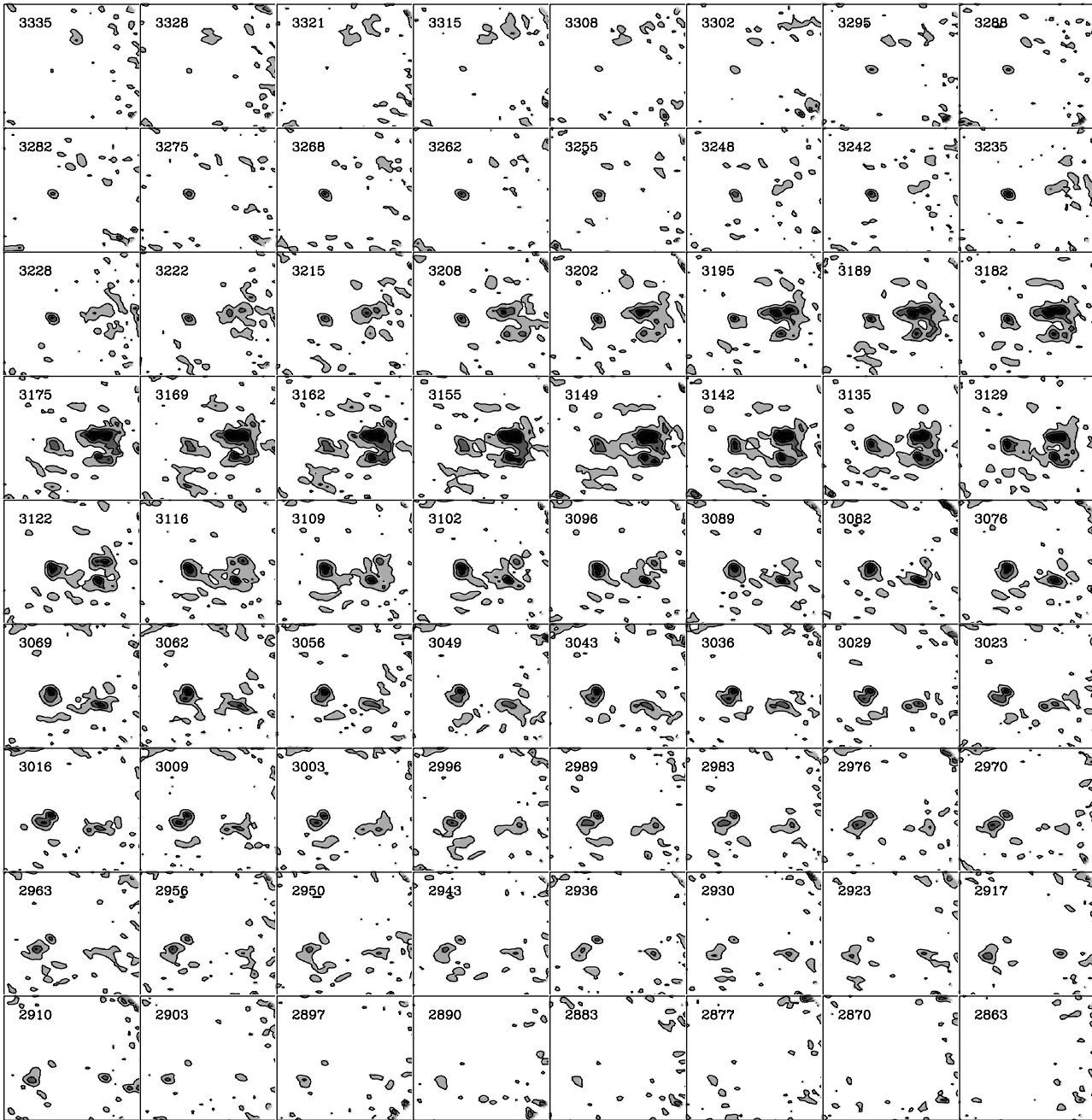


Fig. 9. Channel maps of the $^{12}\text{CO}(1-0)$ emission (combined map). Channel spacing is 6.58 km s^{-1} . Each box is $60''$ in RA and $55''$ in DEC. Levels: from 0.04 to 0.2 Jy/beam by steps of 0.06; the r.m.s. noise level is about 10 mJy/beam.

A2 (the south-east extension of A), B, C and C' are given in Table 3.

Table 3 confirms what is already evident from the simple inspection of the maps: the “nucleus” of NGC 3690, B, is very weak in ^{13}CO emission (compared to ^{12}CO), with ^{13}CO 30 times weaker than ^{12}CO (actually, Fig. 7 suggests that there is no ^{13}CO emission at the very position of B but let us recall that for the computation of the line ratios, the data have been smoothed). C and C' exhibit $^{12}\text{CO}/^{13}\text{CO}$ line ratios that are more typical of ordinary galaxies, in the range 10–15 (Sage & Isbell 1991; Henkel et al. 1991; see also references in Casoli

et al. 1992). As for HCN, it is extremely strong in A with a $^{12}\text{CO}/\text{HCN}$ ratio of 7; actually at this position HCN is 3.5 times stronger than ^{13}CO . In B, HCN emission is still strong relative to $^{12}\text{CO}(1-0)$, with a value of 20, and also 1.6 times stronger than $^{13}\text{CO}(1-0)$. In C and C', the values of the $^{12}\text{CO}/\text{HCN}$ ratio are close to what is observed in the disk of our Galaxy (values of 35–40 have been quoted by Helfer & Blitz 1997b) and HCN becomes weaker than ^{13}CO , which is a more “normal” behavior. As for filament A2, the $^{12}\text{CO}/^{13}\text{CO}$ ratio varies from 10 to 15 and the $^{12}\text{CO}/\text{HCN}$ ratio from 15 to 20.

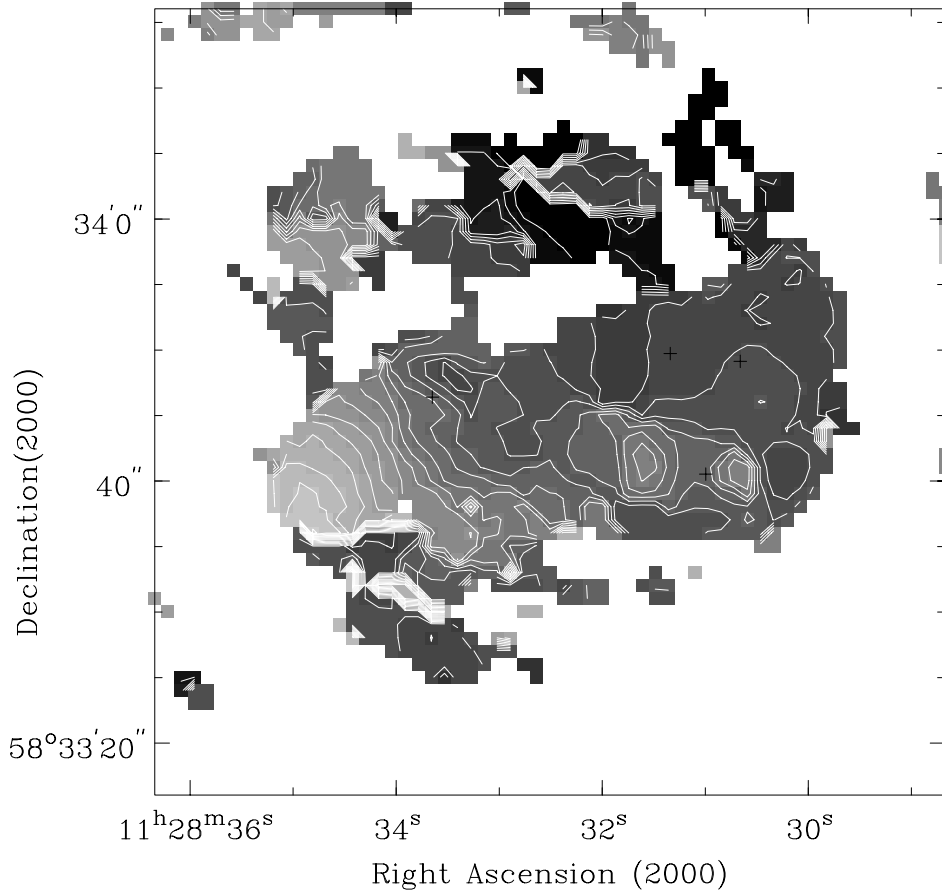


Fig. 10. $^{12}\text{CO}(1-0)$ velocity field in the Arp 299 system (first moment of the line profiles). Crosses mark the positions of A, B1, C and C'. Contours and greyscale run from 2800 (grey) to 3300 km s^{-1} (black) by steps of 20 km s^{-1} . The velocity of A is 3110 km s^{-1} , that of B is 3103 km s^{-1} , C is at 3154 km s^{-1} and C' at 3177 km s^{-1} .

4.5. Comparison with other galaxies

How do these results compare with observations of other galaxies? HCN emission traces the presence of dense gas (a density of about 10^4 cm^{-3} is needed to excite the 1–0 line). Both single-dish and interferometer observations suggest that HCN emission is strong (relative to CO) in galactic bulges, with typical ratios $^{12}\text{CO}(1-0)/\text{HCN}$ around 10 at the 300 pc scale; in disks, the emission ratio is typically 30–40 (see Helfer & Blitz (1997a, 1997b, Nquyen-Q-Rieu et al. 1992, Contini et al. 1997). This is a somewhat schematic description since, even in bulges, this ratio varies a lot from galaxy to galaxy, with values from 2 (NGC 1068) to higher than 30 (Contini et al. 1997).

Matsuhita et al. (1998) have done multiline interferometric observations of the center of M51. Their linear resolution is about 300 pc. They find that in the very center of M51, there is a strong peak of HCN emission which is seen neither in $^{12}\text{CO}(1-0)$, nor in $^{13}\text{CO}(1-0)$. At this position, HCN is stronger than $^{13}\text{CO}(1-0)$ by a factor of 3. This is reminiscent of what we see in both A and B. However, in M51 the $^{12}\text{CO}/^{13}\text{CO}$ ratio is about 8 in the whole nuclear region.

5. Dynamics

The channel maps of $^{12}\text{CO}(1-0)$ emission are given in Fig. 9. One can see clearly that the main regions are all connected; for example, A, B, C and C' all appear in the 3149 km s^{-1}

channel. Therefore the star-forming region C–C' and the nuclear concentrations are likely physically connected. Fig. 10 displays the $^{12}\text{CO}(1-0)$ velocity field, and Fig. 13 the $^{12}\text{CO}(2-1)$ one.

5.1. IC 694 (regions A and C–C')

In the $^{12}\text{CO}(1-0)$ line, the south-east part of A (IC 694) appears not much perturbed (this is also true for HCN), but the western regions exhibit a complex behavior.

Since the velocity field south-east of A appears so regular, we tried to fit a rotation curve to both the CO and HCN data in this region of the galaxy using the task ROTCUR in GIPSY; this task uses the tilted rings model with the position of the rotation center, systemic velocity, the position angle and inclination of the rings as free parameters. Fig. 11 shows the rotation curve computed from both the HCN(1–0) and $^{12}\text{CO}(1-0)$ data for the approaching (SE) side of the galaxy only, using the radio continuum position for the rotation center, $v_{sys} = 3110 \text{ km s}^{-1}$. We have kept the position angle and inclination fixed and equal for both data sets; the best solutions are found for a position angle of $305 \pm 5^\circ$ and an inclination of $70 \pm 5^\circ$. Fig. 11 shows the rotation curves obtained for $\text{PA} = 305^\circ$ and $\text{incl} = 75^\circ$. This regularly rising curve suggests mostly solid rotation and is rather different from the rotation curve of an ordinary spiral galaxy. However the last points are at a radius of $15''$, that is, about 3

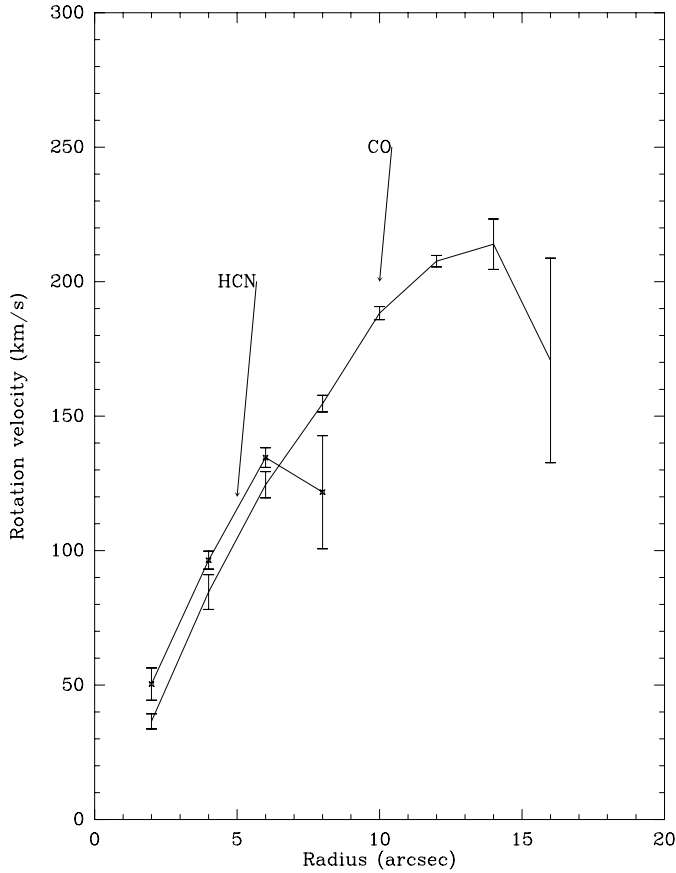


Fig. 11. Rotation curve of IC 694, from the $^{12}\text{CO}(1-0)$ and $\text{HCN}(1-0)$ data. This rotation curve has been fitted for the SE side of IC 694, with the radiocontinuum position as the dynamical center, a position angle of 305° and an inclination to the line of sight of 75° .

kpc only, so that the flat region of the rotation curve may not have been reached (the last point in the curve is less significant, due to the small number of data points at this radius). We note that the $\text{HCN}(1-0)$ points are systematically higher than the $^{12}\text{CO}(1-0)$ ones, an effect that can be attributed in part to the better resolution in the $\text{HCN}(1-0)$ line, but also to the different spatial distributions for HCN and CO , the HCN emitting gas being more confined to the nucleus.

If this curve is to be interpreted as ordered rotation, we can use it to compute the dynamical mass in the central region of A, M_{dyn} . An estimate of M_{dyn} is given by $M_{\text{dyn}} = 2.32 \cdot 10^5 M_\odot R V^2$ where V is in km s^{-1} and R in kpc (Lequeux 1983), thus for $V = 210 \text{ km s}^{-1}$ and $R = 3.2 \text{ kpc}$, the enclosed dynamical mass is $3.3 \cdot 10^{10} M_\odot$. In the same region, the enclosed H_2 mass is about $3 \cdot 10^9 M_\odot$, that is, 9 percent of the dynamical mass. This dynamical mass can also be compared with the value derived in a 0.2 kpc radius by Zhao et al. (1997) which is $7 \cdot 10^8 M_\odot$.

It is rather surprising to find that in this merger, one side of one of the protagonists seems dynamically unperturbed. Indeed, the presence of an extended tidal tail suggests that the interaction has begun some 750 Myr ago (Hibbard & Yun 1996); at $R = 3 \text{ kpc}$, the rotation time is about 100 Myr, and except maybe for

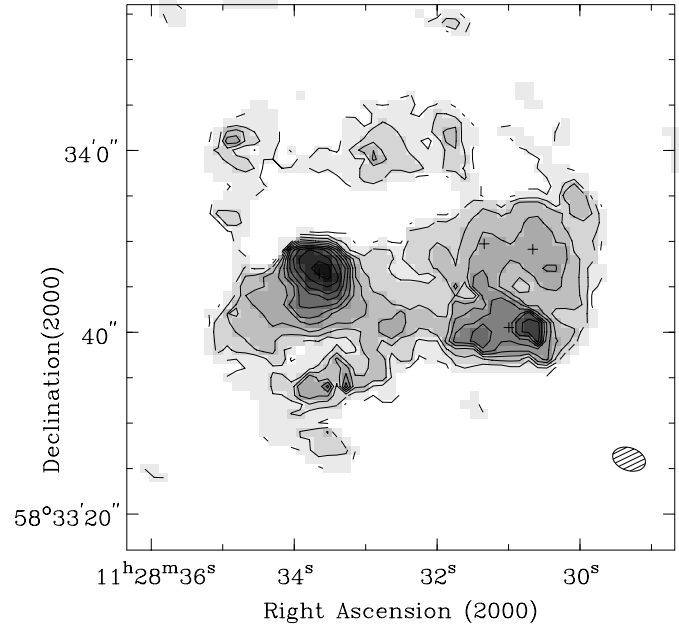


Fig. 12. Map of the $^{12}\text{CO}(1-0)$ velocity dispersion in Arp 299. Note that for a gaussian line, the dispersion is 1.18 times the full-width at half-maximum. Crosses indicate the positions of A, B1, C and C'. Contours and greyscale run from 5 to 105 km s^{-1} by steps of 5 km s^{-1} . Note the large value of the CO linewidth at the position of the IC 694 nucleus (A).

very special geometries, both sides should have felt the effect of the collision. One could then interpret the velocity pattern along the SE part of A as a velocity gradient along a tidal tail; such gradients are observed in the HI tails (Hibbard & van Gorkom 1996) but generally at larger distances from the nucleus. On the other hand, in the merger IRAS 14348-1447 Mihos & Bothun (1998) have found from $\text{H}\alpha$ observations that the two bodies still have coherent rotation. However, IRAS 14348-1447 may have had a different history than Arp 299: although its nuclei are separated by 5 kpc (4.5 kpc for Arp 299), its tidal tails are rather short (20kpc) so that it may be much younger than Arp 299.

The comparison with the HI distribution and kinematics suggest that the velocity pattern that we see in the southern part of IC 694 is part of the overall dynamics of the system. At $22''$ resolution, the HI distribution is elongated (Hibbard & Yun 1999). It includes both galaxy bodies and shows a regular velocity pattern with the approaching side in the SE part of A, as we see in CO, and perturbations related to B. Note that in HI as in CO, C and C' seem to follow these general kinematical trends and to be part of IC 694; the perturbed regions are rather between A and C', and around B, so that speaking of C-C' as the "overlap" region could be improper.

The velocity widths give us some further indications. The map of the second moment of the $^{12}\text{CO}(1-0)$ line is shown in Fig. 12. Linewidths in C and C' are only $20-40 \text{ km s}^{-1}$, more typical of star-forming regions than of galactic nuclei. The maximum value (110 km s^{-1}) is found at the position of the nucleus of IC 694 (A); this maximum is elongated perpendicular to the maximum velocity gradient as expected from resolution effects

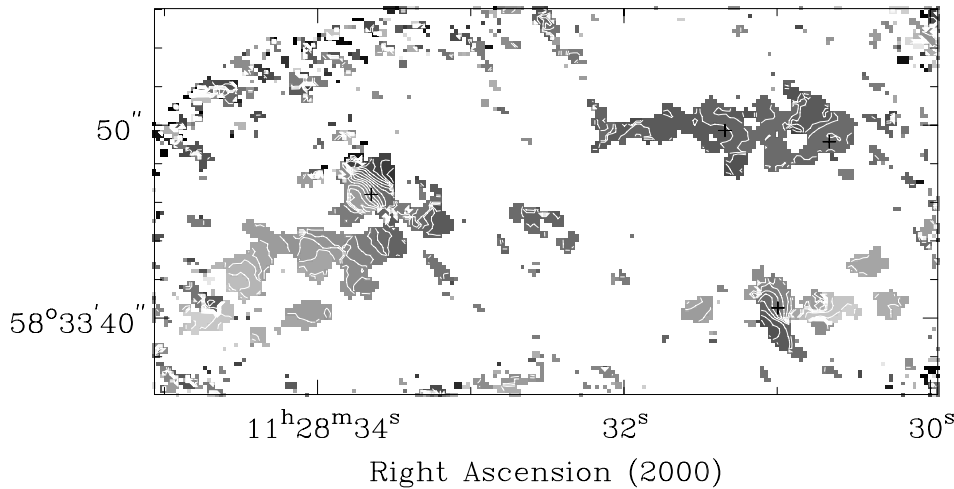


Fig. 13. $^{12}\text{CO}(2-1)$ velocity field in the Arp 299 system (first moment of the line profiles). Crosses mark the positions of A, B1, C and C'. Contours and greyscale run from 2800 (grey) to 3400 km s^{-1} (black) by steps of 20 km s^{-1} .

for rotating disks. Here however we may be seeing a different component, possibly associated with the circumnuclear disk of $2''$ diameter seen in the $\text{H}2\alpha$ line by Zhao et al. (1997), which has a rotational velocity of about 125 km s^{-1} . The dynamical mass associated with this disk is of the order of $7 \cdot 10^8 M_{\odot}$. Note that the PA of the large-scale emission seen in CO, 305° , is consistent with the PA derived for the recombination line at the 200 pc scale, 315° .

5.2. NGC 3690 (region B) and its connections with IC 694

The dynamical status of B, which is supposed to be the nucleus of NGC 3690, is less clear. In the $^{12}\text{CO}(1-0)$ and HCN lines, there is no discernible classical pattern of rotation, although both integrated emission maps show elongated, disk-like structures around B. The $^{12}\text{CO}(2-1)$ map and velocity field (Fig. 13) bring new information on the dynamical status of NGC 3690: first, we see that the disk-like structure around NGC 3690 is actually composed of a concentration on B1 and of two knots of emission east and west of B1; second, the strong gradient observed in this line around the B1 position clearly shows that there is indeed rotation, and that the dynamical center is B1 and not B2. This answers the questions raised in particular by Smith et al. (1996) and Wynn-Williams et al. (1991). The two knots do not share this pattern of rotation, which is not surprising if, as we are going to discuss, they correspond to gas flowing from one region of the galaxy to another.

The $^{12}\text{CO}(1-0)$ spectra in the region around B are complex with several components. To investigate this, we made a position-velocity cut in the $^{12}\text{CO}(1-0)$ data cube between A and B (Fig. 14). This cut reveals first the very wide lines in A, which maybe associated to a circumnuclear disk (see previous section). Second, we see at the position of B1 a rather wide line, which in agreement with the rotation pattern seen in the high-resolution $^{12}\text{CO}(2-1)$ map, and further along the cut, near $-26''$ offset, there are multiple components which seem dynamically associated with C (see the channel map at a velocity of 3155 km s^{-1} in Fig. 9). This explains the features seen in the map of the first line moment.

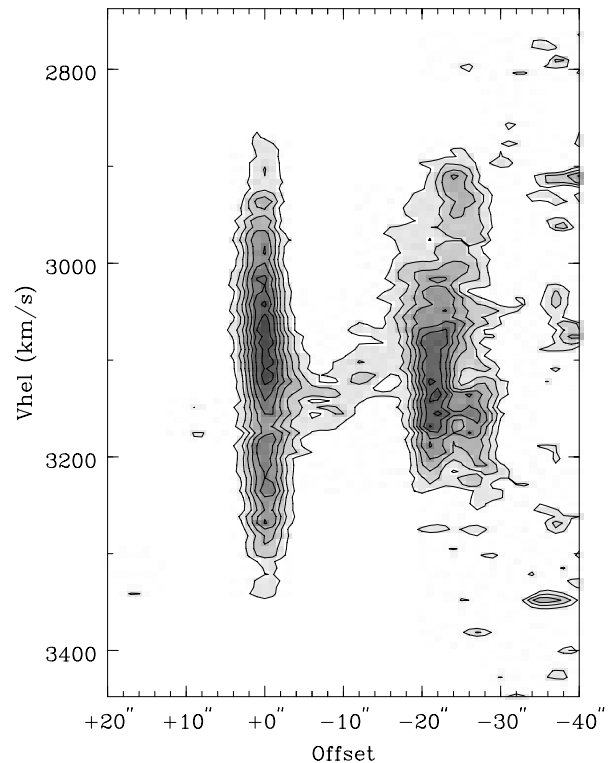


Fig. 14. $^{12}\text{CO}(1-0)$ position-velocity cut in the Arp 299 system, made along the direction going from A to B. Contours and greyscale run from 0.03 to 0.3 Jy/beam by steps of 0.03. The positions are given in arcsec along the cut, A being at an offset of $0''$ and B1 at $-21.5''$.

The most interesting feature of this map is the emission which joins the two regions, going from an offset of $-6''$ and a velocity of 3150 km s^{-1} , to offsets around $-28''$ and velocities of 2900 km s^{-1} . This feature highly suggests gas transfer between the two bodies. Moreover, there is a characteristic depression in the emission of A just at the beginning of the feature which clearly indicates that gas is flowing from A to B. The perturbed shape of the contours in the region where this gas reaches B shows that there is actual interaction with B, and not only a superposition of the two components.

6. Discussion and conclusions

The ^{12}CO maps that we have obtained show an overall good correspondence with the NIR maps of the H_2 and $\text{Br}\gamma$ lines (Willaime et al., in preparation) as well as that of the 8.3 GHz continuum of Zhao et al. (1997). This indicates that at the resolution of several hundred parsecs, molecular complexes and star-forming regions are associated. However there are some striking small-scale differences visible even with the relatively low resolution of the $^{12}\text{CO}(1-0)$ map. In particular, the source B2 (see Fig. 1) is remarkably absent from our millimeter molecular lines maps, while it is very strong in the NIR, both continuum and lines. It is however difficult to go further with the present data, which are at a significantly lower resolution than the NIR maps. A detailed comparison with the sub-arcsec $^{12}\text{CO}(2-1)$ data will be given in a forthcoming paper.

From the point of view of the line ratios, we have seen two different behaviors in Arp 299:

- “nuclear” regions, with HCN stronger than ^{13}CO ; in A HCN is anomalously strong, while in B ^{13}CO is anomalously weak relative to CO;
- “disk” regions: A2, C, C'. The complex C–C' is more likely than A and B to contain gas coming from the external regions of the parent galaxies. Thus it seems that the differences in the observed line ratios compared to an ordinary spiral galaxy are to be searched towards peculiar physical conditions in the nuclei, and not abnormal abundance ratios such as the presence of large amounts of unprocessed gas. LVG models are not very useful to interpret the line ratios since it is clear that filling factors effects are important, especially in comparing ^{12}CO and HCN; however they indicate that A and B contain large amounts of dense and warm gas. Observations of several transitions of ^{13}CO would be useful in this respect, as well as C^{18}O if not too weak.

The large variations of the molecular line ratios across the body of Arp 299 remind us that in such a perturbed system, the computation of H_2 column densities from CO data is a perilous exercise. In any case, our conclusion about the large H_2 mass in the C–C' region, where the ISM is less perturbed than in A and B, is probably sound. If, as it is likely, H_2 masses are overestimated in the nuclear regions A and B, this conclusion will be re-enforced.

These observations also confirm that in an ongoing merger, not all the star formation happens in the galaxy nuclei. The galaxy nuclei, A and B, are indeed regions of bright CO emission, however one third of the emission comes from the third activity center, C–C'. In addition, we have also found that about half of the gas is in weak extended emission not detected with the interferometer.

In a previous paper (Casoli et al. 1989), we had made the hypothesis that C–C' represented the nucleus of a third partner in the collision. In view of these new data, this hypothesis seems less likely. In this region, the CO linewidths are small, which is not typical of a galaxy nucleus, unless seen very close to face-on; in addition, the CO velocity field shows a continu-

ity between the (surprisingly) regular velocity field of A and the C–C' region; this region is then likely what remains of the north-west part of IC 694. Finally, while the molecular line ratios display peculiar values in A and B, they are closer to what can be expected from a galactic disk in C–C': for example, the $^{13}\text{CO}/\text{HCN}(1-0)$ ratio is larger than 1 in the nuclei, and around 2 in C, C' and the SE region of A. All this points towards C–C' being a starburst region probably at the interface between the galaxies. Let us point however that this star-forming region, with several $10^9 M_\odot$ of H_2 and a star-forming activity which is comparable to that around the galaxy nuclei, is rather unusual compared with what is found in spiral galaxies. However, such star-forming regions might be more common in interacting objects, as suggested by the recent ISO results in another on-going merger, the Antennae, where a very intense starburst is found in an off-nuclear region (Mirabel et al. 1998).

The importance of extra-nuclear star-forming regions for the total star formation rate has rarely been pointed by numerical simulations. This may depend upon the collision parameters; indeed in this case the presence of both a faint optical tail and of a huge HI tail suggest that the encounter began 750 Myr ago. In very fast mergers as those studied in numerical simulations, it is possible that most of the gas quickly falls towards the nuclei and forms stars there.

Our observations demonstrate that mergers are a very efficient way to mix the gaseous bodies of the progenitors. The huge off-nucleus gas concentration that we see in C–C' is likely fed by both nuclei, since we observe gas flows between this region and the two nuclei. In addition, there is also gas transfer from one of the nucleus (A) to the second one (B). We are thus witnessing in Arp 299 that even at this not very advanced stage of the merger, the two gaseous bodies have already lost a large part of their individuality.

Acknowledgements. We thank the operators on Plateau de Bure for their help in observing. We wish to thank the IRAM staff in Grenoble for their help in the data reduction, and especially Anne Dutrey, Frédéric Gueth, and Stéphane Guilloteau.

References

- Aalto S., Black J.H., Johansson L.E.B., Booth R.S., 1991, A&A 249, 323
 Aalto S., Radford S.J.E., Scoville N.Z., Sargent A.I., 1997, ApJ 475, L107
 Barnes J.E., Hernquist L., 1996, ApJ 471, 115
 Braine J., Dumke M., 1998, A&A 333, 38
 Casoli F., Combes F., Augarde R., Figon P., Martin J.M., 1989, A&A 224 31
 Casoli F., Dupraz C., Combes F., 1992, A&A 264, 55
 Clements D.L., Baker A.C., 1996, A&A 314, L5
 Clements D.L., Sutherland W.J., MacMahon R.G., Saunders W., 1996, MNRAS 279, 477
 Condon J.J., Helou G., Sanders D.B., Soifer B.T., 1990, ApJS 73, 359
 Contini T., Wozniak H., Considere S., Davoust E., 1997, A&A 324, 41
 Dudley C.C., Wynn-Williams C.G., 1993, ApJ 407, L65
 Gehrz R.D., Sramek R.A., Weedman D.W., 1983, ApJ 267, 551
 Goldader J.D., Joseph R.D., Doyon R., Sanders D.B., 1997, ApJ 471, 104

- Guilloteau S., Delannoy J., Downes D., et al., 1992, *A&A* 262, 624
- Helfer T., Blitz L., 1997a, *ApJ* 478, 162
- Helfer T., Blitz L., 1997b, *ApJ* 478, 233
- Henkel C., Mauersberger R., Baan W.A., 1991, *A&AR* 3, 47
- Hibbard J., van Gorkom J., 1996, *AJ* 111, 655
- Hibbard J.E., Yun M.S., 1996, In: Bremer M.N., van der Werf P.P., Røttgering H.J.A., Carilli C.L. (eds.) *Cold Gas at High Redshift*. Kluwer Academic Publishers
- Hibbard J.E., Yun M.S., 1999, *AJ*, submitted for publication
- Keto E., Hora J.L., Deutsch L., et al., 1997, *ApJ* 485, 598
- Lequeux J., 1983, *A&A* 125, 394
- Matsuhita S., Kohno K., Vila-Vilaro B., Tosaki T., Kawabe R., 1998, *ApJ* 495, 267
- Mihos J.C., Hernquist L., 1996, *ApJ* 464, 641
- Mihos J.C., Bothun G.D., 1998, *ApJ* 500, 619
- Mirabel I.F., Vigroux L., Charmandaris V., et al., 1998, *A&A* 333, L1
- Nguyen-Q-Rieu, Jackson J., Hemkel C., Truong-Bach, Mauersberger R., 1992, *ApJ* 399, 521
- Sage L.J., Isbell D.W., 1991, *A&A* 249, 31
- Sargent A.I., Scoville N.Z., 1991, *ApJ* 366, L1
- Sargent A.I., Sanders D.B., Scoville N.Z., Soifer B.T., 1987, *ApJ* 312, L35
- Shier L.M., Rieke M.J., Rieke G.H., 1996, *ApJ* 470, 222
- Smith D.A., Herter T., Haynes M.P., Beichman C.A., Gautier T.N., 1996, *ApJS* 104, 217
- Smith H.E., Lonsdale C.J., Lonsdale C.J., 1998, *ApJ* 492 137
- Solomon P.M., Sage L.J., 1988, *ApJ* 334, 613
- Solomon P.M., Downes D., Radford S.J.E., 1992 *ApJ* 387, L55
- Wynn-Williams C.G., Eales S.A., Becklin E.E., et al., 1991, *ApJ* 377, 426
- Zhao J.-H., Anantharamaiah K.R., Goss W.M., Viallefond F., 1997, *ApJ* 482, 186